

Transport Signatures of Inverted Andreev Bands in Topological Josephson Junctions

Jonathan Sturm,¹ Raffael L. Klees,^{1,2} Ewelina M. Hankiewicz,¹ and Daniel Gresta¹

¹*Institute for Theoretical Physics and Astrophysics and Würzburg-Dresden Cluster of Excellence *ct.qmat*, Julius-Maximilians-Universität Würzburg, 97074 Würzburg, Germany*

²*Institute of Physics, University of Augsburg, D-86159 Augsburg, Germany*

(Dated: January 3, 2025)

We study the thermoelectrical transport transverse to conventional and topological Josephson junctions with a central quantum dot (QD). For that purpose, we derive an effective resonant tunneling model where the QD is renormalized with an induced superconducting gap. By applying Keldysh Green's function technique, we compute the local density of states as well as the transmission functions. In the latter case, we observe that the Andreev bound states forming on the QD are inverted if the junction has p -wave symmetry, meaning that electron and hole orbitals switch roles. We calculate the thermoelectric transport coefficients both analytically and numerically and show how the induced gaps and the band inversion are reflected in the electrical and heat conductance as well as the Seebeck coefficient, the latter experiencing a sign change in the topological case.

I. INTRODUCTION

Two decades ago, the seminal work by Kitaev [1] predicted the presence of Majorana zero modes (MZMs) at the boundaries of spinless superconductors (SCs) with p -wave pairing symmetry. However, the experimental verification of their existence is still an open problem. Although it is a well established fact that coupling a metal electrode to a MZM leads to a zero voltage conductance peak [2–5], it has been shown that such a peak is not an exclusive feature of MZMs but can be generated by any zero-energy mode [6–9].

By coupling two p -wave SCs to each other, a topological Josephson junction (JJ) is formed. The interference of the two Majorana fermions induces a MZM in the Andreev bound states (ABS) at a phase difference of π , leading to a 4π -periodic Josephson current [10–13]. However, also this MZM signature turned out to be ambiguous as it can be mimicked by topologically trivial JJs [14, 15].

In search of alternative ways to prove the existence of MZMs in topological SC structures, thermal and thermoelectric transport have proven themselves powerful tools. For heat transport, it has been shown that the thermal conductance along a topological JJ is quantized [10, 16] and that the 4π -periodic ground-state fermion parity can be measured in phase-dependent thermodynamics [17]. Moreover, several studies have found a sign change in the Seebeck coefficient of a resonant tunneling model (RTM), that is, a normal metal-quantum dot-normal metal structure, when the quantum dot (QD) is coupled to a MZM [18–20]. However, so far no intuitive physical explanation for this anomalous Seebeck effect has been given.

In this work, we address this problem by tracing back the sign change to a band inversion on the QD by showing that electron and hole orbitals exchange roles. For that, we extend the RTM by coupling two additional SC leads to the QD, obtaining the four-terminal structure shown in Fig. 1 (a). The two SCs, which will be of s - or p -wave type, induce ABS on the QD, which can be probed by transverse transport between the normal leads. Such a

geometry has been successfully used in a previous work [21] to theoretically show that the transverse heat conductance in a topological junction is quantized.

This paper is organized as follows: In Section II, we set the theoretical stage by stating the mathematical model and explaining the nonequilibrium Green's function formalism used to compute the transport observables. In Section III, we analyze the local density of states and the transmission functions of the different transport processes to reveal the band inversion. We show how the band inversion can be measured in the differential conductance as well as the Seebeck coefficient in Section IV. Finally, in Section V we give a short summary of our findings and an outlook to future directions in this field.

II. SETUP AND FORMALISM

A. Model

The system under consideration is a four-terminal junction consisting of two SC leads (S) with labels $\{1, 2\}$ and two normal metallic electrodes (N) labeled by $\{L, R\}$ that are all coupled to a central QD with energy level ε_0 , cf. Fig. 1 (a). With that, an S-QD-S Josephson junction is formed in the vertical direction, while on the horizontal we have an N-QD-N resonant tunneling model. Both systems separately have been studied extensively in the literature, see eg. Refs. [22] and [23], respectively. The coupling to the S leads induces ABS on the QD, which depend on the phase difference $\phi = \varphi_1 - \varphi_2$ between the SCs and can be modified with the energy level of the QD ε_0 . These ABS in turn define an effective RTM with a superconducting QD (cf. Fig. 1 (b)) that can be probed by means of thermoelectric transport between the normal leads, which is the central goal of this article.

The Hamiltonian describing the full system is given by

$$H = H_S^\alpha + H_N + H_T + H_0 . \quad (1)$$

$H_S^\alpha = H_1^\alpha + H_2^\alpha$ is the Hamiltonian of the SC leads 1 and 2. The index $\alpha \in \{s, p\}$ indicates the pairing symmetry

of the SC leads. If $\alpha = s$, both leads are of s -wave symmetry, forming a conventional JJ, while for $\alpha = p$, $H_{1,2}^p$ describe a pair of semi-infinite Kitaev chains [1, 24], leading to a topological JJ. Therefore, in the case $\alpha = p$ we consider the whole system to be fully spin-polarized. $H_N = H_L + H_R$ models the normal metallic leads L,R. The tunneling between the QD and the leads is given by the Hamiltonian

$$H_T = \sum_{i=1,2,L,R} \sum_{\sigma} t_i \left(c_{0\sigma}^{\dagger} c_{i\sigma} + c_{i\sigma}^{\dagger} c_{0\sigma} \right), \quad (2)$$

with hopping amplitudes $t_i \in \mathbb{R}$. Here, $c_{i\sigma}^{(\dagger)}$ and $c_{0\sigma}^{(\dagger)}$ are the fermionic operators of lead i and the QD, respectively. In the case $\alpha = s$, the spin index takes values $\sigma = \uparrow, \downarrow$, while for $\alpha = p$ we choose the polarization as $\sigma = \uparrow$. Lastly, the QD is assumed to be spin-degenerate and non-interacting with a single energy level ε_0 , yielding the Hamiltonian

$$H_0 = \sum_{\sigma} \varepsilon_0 c_{0\sigma}^{\dagger} c_{0\sigma}. \quad (3)$$

The physics of the boundaries of the leads that are connected to the QD are fully contained in their boundary Green's functions (GFs). We use the Nambu basis spinors $\psi_i^{\dagger} = (c_{i\uparrow}^{\dagger}, c_{i\downarrow})$ ($i \in \{1, 2, L, R, 0\}$), whereby the spin index is only present in the case $\alpha = s$. With that, the boundary GFs for the S leads in the wide-band limit read [24]

$$g_{1,2}^s(\varepsilon) = -\pi\nu_0 \frac{\varepsilon\tau_0 + \Delta e^{i\varphi_{1,2}}\tau_1}{\sqrt{\Delta^2 - \varepsilon^2}}, \quad (4a)$$

$$g_{1,2}^p(\varepsilon) = \frac{\pi\nu_0}{\varepsilon} \left(\sqrt{\Delta^2 - \varepsilon^2}\tau_0 \pm \Delta e^{i\varphi_{1,2}}\tau_1 \right). \quad (4b)$$

Here, $\Delta > 0$ is the SC gap, $\varphi_{1,2}$ are the SC phases, and ν_0 is the density of states at the Fermi level in the normal-conducting state. $\tau_{j=0,\dots,3}$ are the identity and Pauli matrices in Nambu space. The sign change of Δ between g_1^p and g_2^p is a direct consequence of the antisymmetry of the p -wave pairing [24], while the s -wave pairing is symmetric and, therefore, there is no sign change between g_1^s and g_2^s . We will show how this can be used to measure the pairing symmetry and characterize the junction below. The corresponding retarded and advanced GFs, $g_{1,2}^{\alpha,r/a}$, are obtained by shifting $\varepsilon \mapsto \varepsilon \pm i\eta$, where $\eta > 0$ is the Dynes parameter [25], which phenomenologically accounts for small disorder. The GFs for the normal leads then follow by taking the limit $\Delta \rightarrow 0$ [23]:

$$g_{L,R}^{r/a} = \lim_{\Delta \rightarrow 0} g_{1,2}^{\alpha,r/a}(\varepsilon) = \mp i\pi\nu_0\tau_0. \quad (5)$$

Finally, the couplings in Nambu space read $V_{i0} = V_{0i} = t_i\tau_3$ and the Hamiltonian of the QD is $\mathcal{H}_0 = \varepsilon_0\tau_3$.

B. Self-energies and induced gaps

For the transport formalism that we will make use of below, we need the dressed GF of the QD, G_0^{α} , which can

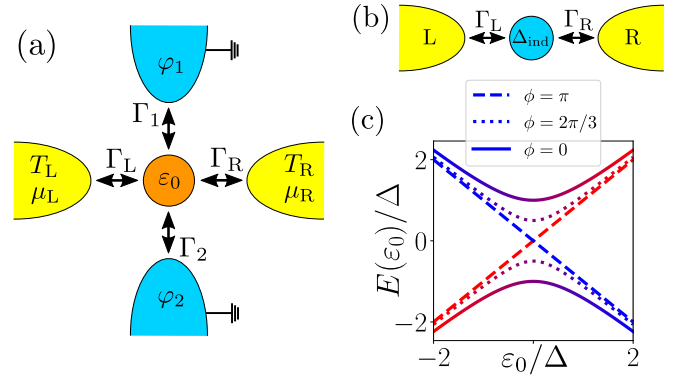


FIG. 1. (a) Two SCs (blue) with phases $\varphi_{1,2}$ and two normal leads (yellow) with chemical potentials $\mu_{L,R}$ and temperatures $T_{L,R}$ are coupled to a QD with energy level ε_0 (orange) via couplings $\Gamma_{1,2}$ and $\Gamma_{L,R}$. The SCs are grounded, implying $\mu_{1,2} \equiv 0$. (b) Effective RTM with a superconducting QD with induced pairing Δ_{ind} . (c) Quasiparticle excitation spectrum $E = \pm\sqrt{\varepsilon_0^2 + |\Delta_{\text{ind}}^s|^2}$, cf. Eq. (11) and the discussion thereunder, for various phase differences $\phi = \varphi_1 - \varphi_2$. The red (blue) segments indicate electron-like (hole-like) quasiparticles. The particle hole mixing is indicated by the color gradient. We used $\Gamma_1 = \Gamma_2 = \Delta/2$.

be found from the Dyson equation as

$$G_0^{\alpha} = (\varepsilon - \mathcal{H}_0 - \Sigma_S^{\alpha} - \Sigma_N)^{-1}. \quad (6)$$

The self-energy originating from the normal leads is given by

$$\Sigma_N = \sum_{i=L,R} V_{0i} g_i^{\alpha} V_{i0} = -i(\Gamma_L + \Gamma_R)\tau_0, \quad (7)$$

where we defined $\Gamma_i = \pi\nu_0 t_i^2$. In the same way one can obtain the self-energies from the coupling to the SCs, $\Sigma_S^{\alpha} = \sum_{i=1,2} V_{0i} g_i^{\alpha} V_{i0}$, whose explicit forms are

$$\Sigma_S^s(\varepsilon) = \begin{pmatrix} -\tilde{\varepsilon}(\Gamma_1 + \Gamma_2) & \Delta_{\text{ind}}^s \\ (\Delta_{\text{ind}}^s)^* & -\tilde{\varepsilon}(\Gamma_1 + \Gamma_2) \end{pmatrix}, \quad (8a)$$

$$\Sigma_S^p(\varepsilon) = \begin{pmatrix} \tilde{\varepsilon}^{-1}(\Gamma_1 + \Gamma_2) & \Delta_{\text{ind}}^p \\ (\Delta_{\text{ind}}^p)^* & \tilde{\varepsilon}^{-1}(\Gamma_1 + \Gamma_2) \end{pmatrix}, \quad (8b)$$

where $\tilde{\varepsilon} = \frac{\varepsilon}{\sqrt{\Delta^2 - \varepsilon^2}}$. As the off-diagonal terms $\Delta_{\text{ind}}^{\alpha}$ induce mixing of particles and holes, we call them induced gaps, which have the form

$$\Delta_{\text{ind}}^s = \frac{\Delta}{\sqrt{\Delta^2 - \varepsilon^2}} (\Gamma_1 e^{i\varphi_1} + \Gamma_2 e^{i\varphi_2}), \quad (9a)$$

$$\Delta_{\text{ind}}^p = -\frac{\Delta}{\varepsilon} (\Gamma_1 e^{i\varphi_1} - \Gamma_2 e^{i\varphi_2}). \quad (9b)$$

Notice that while the induced s -wave gap Δ_{ind}^s is symmetric under exchange of the two SCs, Δ_{ind}^p is antisymmetric. This property is inherited from the signs of the pairing terms in the GFs in Eq. (4) and hence, as pointed out above, a direct consequence of the different pairing

symmetries. To make this property more evident, we consider the absolute values of $\Delta_{\text{ind}}^\alpha$, yielding

$$|\Delta_{\text{ind}}^s|^2 \propto (\Gamma_1 - \Gamma_2)^2 + 4\Gamma_1\Gamma_2 \cos^2(\phi/2), \quad (10a)$$

$$|\Delta_{\text{ind}}^p|^2 \propto (\Gamma_1 - \Gamma_2)^2 + 4\Gamma_1\Gamma_2 \sin^2(\phi/2). \quad (10b)$$

Therefore, $|\Delta_{\text{ind}}^s|$ ($|\Delta_{\text{ind}}^p|$) is minimal (maximal) for $\phi = \pi$ ($\phi = 0$), while being maximal (minimal) for $\phi = 0$ ($\phi = \pi$). The strong dependence of the induced gap on the phase difference, which originates from the interference of the ground-state wavefunctions of the SC leads, can be used to control the mixing of particles and holes on the QD. To illustrate this, consider the s -wave case in the low-energy limit $\varepsilon/\Delta \rightarrow 0$, allowing us to define an effective Hamiltonian \mathcal{H}_{eff} of the QD as

$$\mathcal{H}_{\text{eff}} = \mathcal{H}_0 + \Sigma_S^s(0) = \begin{pmatrix} \varepsilon_0 & \tilde{\Delta}_{\text{ind}}^s \\ (\tilde{\Delta}_{\text{ind}}^s)^* & -\varepsilon_0 \end{pmatrix}, \quad (11)$$

where now $\tilde{\Delta}_{\text{ind}}^s = \Gamma_1 e^{i\varphi_1} + \Gamma_2 e^{i\varphi_2}$. The spectrum of this Hamiltonian is then given by $E = \pm \sqrt{\varepsilon_0^2 + |\tilde{\Delta}_{\text{ind}}^s|^2}$, which is shown in Fig. 1 (c) for the case $\Gamma_1 = \Gamma_2$. As one can see, the quasiparticle excitation spectrum on the QD (i.e., the ABS) as a function of ε_0 resembles the common spectrum of an s -wave SC with the additional parameter ϕ enabling to open and close the gap. With that, the phase difference allows us to continuously transform the effective N-S-N-junction in Fig. 1 (b) ($\phi \neq \pi$) into a standard RTM ($\phi = 0$). Note that if $\Gamma_1 \neq \Gamma_2$, this statement still holds approximately if the deviation is small ($|\Gamma_1 - \Gamma_2|/\Gamma_1 \ll 1$), which is the case we are interested in. This will help us to interpret the ABS and transmission functions below.

C. Transport formalism

Different from many transport studies of JJs, we are interested in the thermoelectric transport between the two normal leads rather than the Josephson current along the JJ. This approach has several advantages: Firstly, we can study the electrical conductance without applying a voltage bias between the SCs and avoid driving the system in a fully nonequilibrium state [26]. Secondly, we can study thermoelectric effects by heating the metallic leads rather than the SCs, which is favorable from the experimental point of view. Thirdly, the transverse approach allows us to directly study the subgap physics rather than the quasiparticle transport above the gap.

To do so, we define the electrical and heat currents in the left lead by means of the Heisenberg equation of motion as $I_L = \frac{e}{\hbar} \langle [H, N_L] \rangle$ and $J_L = -\frac{1}{\hbar} \langle [H, H_L - \mu_L N_L] \rangle$, respectively, where $e > 0$ is the elementary charge, \hbar is the reduced Plack constant, and $N_L = \sum_\sigma c_{L\sigma}^\dagger c_{L\sigma}$ is the particle number operator of the left lead. Let $\mu_{L,R}$ and $T_{L,R}$ be the chemical potentials and temperatures of the left and right leads, respectively. Since we assume the SCs to be grounded, we

set their chemical potentials $\mu_{1,2} \equiv 0$. Moreover, we set $\mu_L = \mu + \Delta\mu$ and $\mu_R = \mu$, as well as $T_L = T + \Delta T$ and $T_R = T$. In a linear response regime, where $\Delta\mu \ll k_B T$ and $\Delta T \ll T$ are small compared to the reference temperature T (k_B is the Boltzmann constant), the currents are related to the biases by means of the Onsager matrix (cf. Appedix B) [27]:

$$\begin{pmatrix} I_L/e \\ J_L/(k_B T) \end{pmatrix} = \frac{1}{h} \begin{pmatrix} L_{11}^\alpha & L_{12}^\alpha \\ L_{21}^\alpha & L_{22}^\alpha \end{pmatrix} \begin{pmatrix} \Delta\mu \\ k_B \Delta T \end{pmatrix}, \quad (12)$$

where $L^\alpha = (L_{ij}^\alpha)_{i,j=1,2}$ is the Onsager matrix whose coefficients are given by

$$L_{ij}^\alpha = \int_{-\infty}^{\infty} \left(\frac{\varepsilon - \mu}{k_B T} \right)^{i+j-2} \mathcal{T}_{ij}^\alpha(\varepsilon) \left(-\frac{\partial f}{\partial \varepsilon} \right) d\varepsilon, \quad (13)$$

with the Fermi function $f(\varepsilon) = (1 + \exp(\frac{\varepsilon - \mu}{k_B T}))^{-1}$. As we show in Appendix A, the transmission functions are given by

$$\mathcal{T}_{11}^\alpha = \mathcal{T}_{21}^\alpha = \mathcal{T}_{\text{EC}}^\alpha + \mathcal{T}_{\text{CAR}}^\alpha + 2\mathcal{T}_{\text{AR}}^\alpha, \quad (14a)$$

$$\mathcal{T}_{12}^\alpha = \mathcal{T}_{22}^\alpha = \mathcal{T}_{\text{EC}}^\alpha + \mathcal{T}_{\text{CAR}}^\alpha, \quad (14b)$$

satisfying the Fisher-Lee relations [28]

$$\mathcal{T}_{\text{AR}}^\alpha = 4\Gamma_L^2 |G_0^{\alpha,\text{eh}}|^2, \quad (15a)$$

$$\mathcal{T}_{\text{EC}}^\alpha = 4\Gamma_L \Gamma_R |G_0^{\alpha,\text{ee}}|^2, \quad (15b)$$

$$\mathcal{T}_{\text{CAR}}^\alpha = 4\Gamma_L \Gamma_R |G_0^{\alpha,\text{eh}}|^2. \quad (15c)$$

The three transmission functions describe the probabilities of three transport processes: $\mathcal{T}_{\text{AR}}^\alpha$ is the probability of Andreev reflection (AR), i.e., converting an electron from the left lead into a hole in the same lead. The elastic cotunneling (EC) probability is given by $\mathcal{T}_{\text{EC}}^\alpha$ and is the usual tunneling of an electron from the left to the right lead via the QD. Lastly, crossed Andreev reflection (CAR) is the process of an electron from the left lead being converted into a hole in the right lead with probability $\mathcal{T}_{\text{CAR}}^\alpha$. Note that we only consider subgap transport processes since we are only interested in small biases around the Fermi level $\mu = 0$ and, therefore, can neglect quasiparticle transport above the gap.

There are four different thermoelectric phenomena contained in Eq. (12): The most common one is the generation of an electrical current under a finite bias $\Delta\mu \neq 0$ while $\Delta T = 0$, which is described by the electrical conductance G^α . Under the same conditions also a heat current is flowing, which is known as the Peltier effect with Peltier coefficient Π^α . On the other hand, also a finite temperature gradient $\Delta T \neq 0$ will generate a heat current, where the heat conductance K^α is defined for an electrically insulating system ($I_L = 0$). In this case, a voltage bias forms to balance out the temperature bias such that there is no net charge transport. The formation of this voltage bias is known as the Seebeck effect with Seebeck coefficient (of thermopower) S^α .

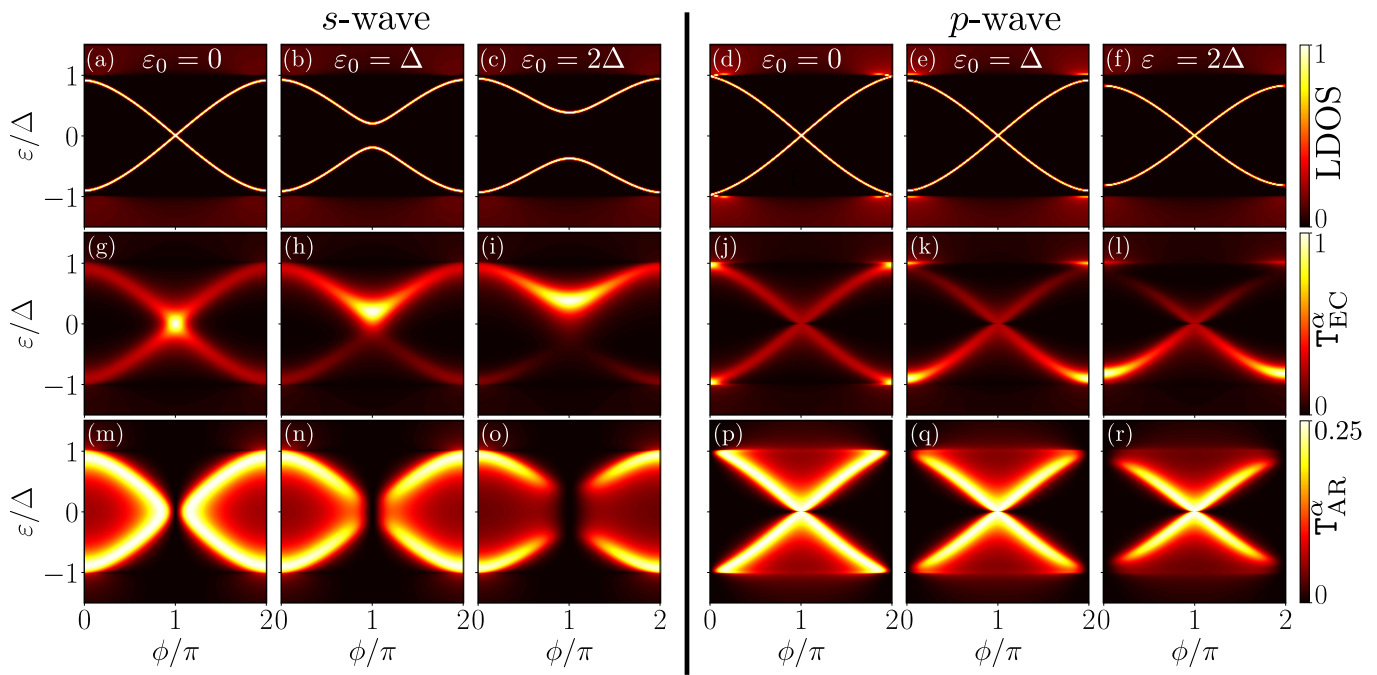


FIG. 2. First row: LDOS on the QD, cf. Eq. (17), as a function of ϕ and ε . We used $\Gamma_1 = \Gamma_2 = 2\Delta$ and $\Gamma_L = \Gamma_R = 0$. Second and third row: T_{EC}^α and T_{AR}^α , respectively. Here we used $\Gamma_1 = \Gamma_2 = 2\Delta$ and $\Gamma_L = \Gamma_R = \Delta/2$. In all plots we used the Dynes parameter $\eta = 0.001\Delta$.

In terms of the Onsager matrix elements, the four transport coefficients are given by

$$G^\alpha = G_0 L_{11}^\alpha, \quad (16a)$$

$$S^\alpha = \frac{k_B}{e} \frac{L_{12}^\alpha}{L_{11}^\alpha}, \quad (16b)$$

$$\Pi^\alpha = \frac{k_B T}{e} \frac{L_{21}^\alpha}{L_{11}^\alpha}, \quad (16c)$$

$$K^\alpha = \frac{3K_0}{\pi^2} \frac{\det(L^\alpha)}{L_{11}^\alpha}, \quad (16d)$$

where $G_0 = e^2/h$ and $K_0 = \pi^2 k_B^2 T / (3h)$ are the quanta of electrical and heat conductance, respectively. Since both T_{AR}^α and T_{CAR}^α are symmetric functions of ε [29], we have $L_{12}^\alpha = L_{21}^\alpha$ and these coefficients only depend on T_{EC}^α . Therefore, we also have $\Pi^\alpha = TS^\alpha$, which is why we only have to discuss the Seebeck effect in addition to electrical and heat conductance.

III. DENSITY OF STATES AND INVERTED ANDREEV BANDS

A. Local density of states and transmission functions

Let us now analyze the ABS forming on the dot. For that, we numerically compute the local density of states

(LDOS) from the GF as

$$\text{LDOS} = -\frac{1}{\pi} \text{Im} \left(G_0^{\alpha,ee} + G_0^{\alpha,hh} \right). \quad (17)$$

The results are shown in Figs. 2 (a)-(c) for the case $\alpha = s$ and (d)-(f) for $\alpha = p$ for different values of the QD energy level ε_0 . Notice that the dot level here takes the role of a scattering potential in the continuum approach [30]: For $\varepsilon_0 = 0$, the ABS gap closes at $\phi = \pi$ (a), increasing the dot level lifts the degeneracy and the gap opens (b)-(c). In contrast, for $\alpha = p$ the degeneracy at $\phi = \pi$ is conserved for any value of ε_0 (d)-(f) and a gap to the continuum opens. This protected zero-energy crossing is the most well-known feature of topological JJs and is often referred to as Majorana bound states.

Now we can study the transmission functions T_{EC}^α and T_{AR}^α , which are defined in Eqs. (15) (a)-(b). As stated above, we use $\Gamma_L = \Gamma_R$, implying $T_{\text{AR}}^\alpha = T_{\text{CAR}}^\alpha$, making it sufficient to discuss T_{AR}^α . We start with the analysis of T_{EC}^α , which is shown in Figs. 2 (g)-(i) for $\alpha = s$ and in (j)-(l) for $\alpha = p$. The transmission is basically given by a broadening of the LDOS with some important details. For $\alpha = s$, there is a maximum of transmission around $\phi = \pi$, which is found at positive energies $\varepsilon > 0$ if $\varepsilon_0 > 0$, cf. (h) and (i). The reason for the location of the maximum lies in the induced gap $|\Delta_{\text{ind}}^s(\phi)|$, which vanishes at $\phi = \pi$ (if $\Gamma_1 = \Gamma_2$) and, hence, there is no particle-hole mixing, leading to a maximal EC transmission. A similar feature can be observed for $\alpha = p$: The induced gap $|\Delta_{\text{ind}}^p(\phi)|$ vanishes at $\phi = 0$, which is why the maximal transmission is found at this point. How-

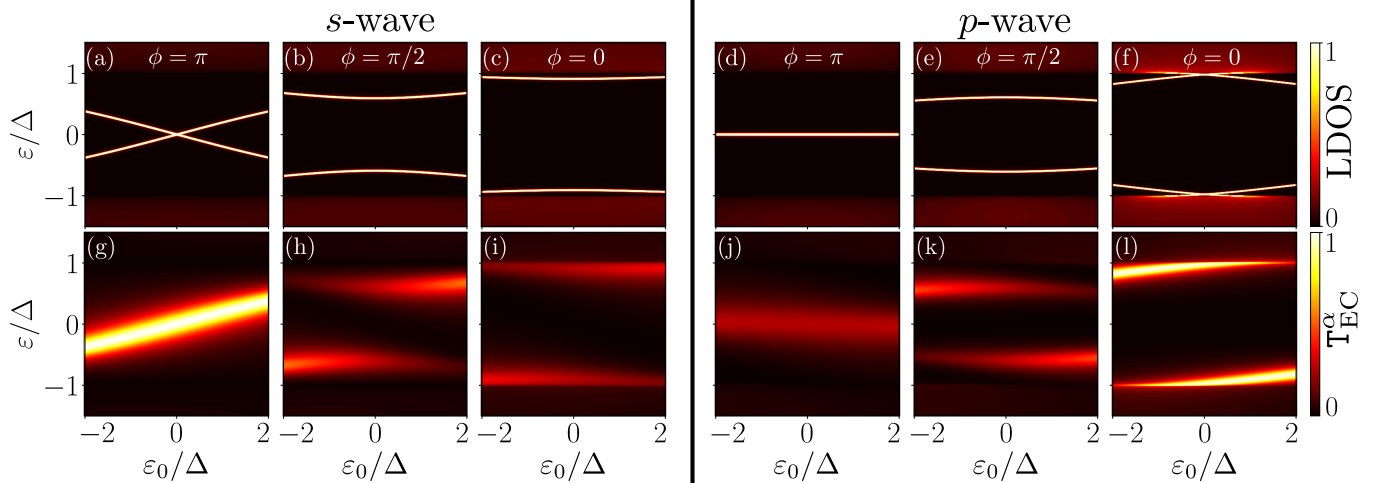


FIG. 3. First row: LDOS on the QD, cf. Eq. (17), as a function of ε_0 and ε . We used $\Gamma_1 = \Gamma_2 = 2\Delta$ and $\Gamma_L = \Gamma_R = 0$. Second row: T_{EC}^α as a function of ε_0 and ε . Here we used $\Gamma_1 = \Gamma_2 = 2\Delta$ and $\Gamma_L = \Gamma_R = \Delta/2$. In all plots we used the Dynes parameter $\eta = 0.001\Delta$.

ever, there is a severe difference to the s -wave case: For finite QD energy $\varepsilon_0 > 0$, the maximal transmission is found at negative energies. This reversed behavior of the EC transmission as function of energy is a first hint towards the band inversion of the ABS, which is the main observation of this paper and will be discussed in more detail the next section.

In contrast to the EC transmission, T_{AR}^α shown in Figs. 2 (m)-(r) is a symmetric function of ε due to particle-hole symmetry. Therefore, band inversion cannot be observed in local or crossed Andreev reflection. The AR transmission has a constant value of 0.25 along the LDOS with exception of the gap vanishing points $\phi = \pi$ for $\alpha = s$ and $\phi = 0$ for $\alpha = p$, where there is no particle-hole mixing and, hence, no Andreev reflection. This can be used for junction characterization: Since at $\phi = \pi$ the AR transmission vanishes in the s -wave case, there will also be zero electrical conductance coming from AR, while for $\alpha = p$ the value will be finite and also quantized as we will show below.

B. Inverted Andreev bands

As we have seen above, the transmission T_{EC}^p shows an anomalous behavior as it has its maximum at negative energies when the dot level is positive. To make this more visible and give it a plausible interpretation, we take a different perspective by revisiting the LDOS and EC transmissions as a function of ε_0 for a fixed phase, which yields the plots in Fig. 3.

We start again by analyzing the LDOS shown in Figs. 3 (a)-(c) for $\alpha = s$ and in (d)-(f) for $\alpha = p$. In the s -wave case, if $\phi = \pi$, the induced gap $|\Delta_{\text{ind}}^s(\phi)|$ vanishes and, hence, the dispersion in panel (a) resembles the bare dot dispersion renormalized by the presence of the quasipar-

ticle continuum at $\varepsilon > \Delta$. As soon as we tune the phase away from π in (b) and (c), the gap opens leading to a particle-hole mixing on the dot, cf. the analytical quasiparticle spectrum in Fig. 1 (c). All in all, the dispersion on the dot for $\alpha = s$ is close to the usual quasiparticle dispersion in an s -wave SC, cf. Fig. 1 (c).

This is very different in the p -wave case. The zero-energy crossing at $\phi = \pi$ now shows as a constant twofold degenerate zero-energy mode. Tuning the phase difference away from π lifts the degeneracy (panels (e) and (f)). Remarkably, the modes have opposite curvature compared to the s -wave case.

Let us now analyze again the EC transmission. Reading T_{EC}^α now as a function of ε_0 allows for an easy distinction of electron-like quasiparticles from hole-like ones: Recall that T_{EC}^α is only computed from the electronic GF. Therefore, the larger the EC transmission the stronger the electronic character of the quasiparticles. This idea is confirmed in Fig. 3 (g). Since the induced gap vanishes in this plot, the EC transmission - up to the aforementioned renormalization due to the above-gap continuum - recovers the usual electron transmission through a resonant level (see, e.g., Ref. [23]). By tuning the phase difference away from π in panels (h) and (i), the induced pairing mixes particles and holes on the dot, whereby the electron-like states are found where the signs of ε and ε_0 match (cf. the red curves in Fig. 1 (c)).

Comparing these findings to the p -wave case shown in panes (j)-(l), one could think at first that here the hole transmission is shown instead of the electrons: The stripe of finite transmission in panel (j) shows a - slight but visible - negative slope, which reminds of the hole transmission in an RTM. Moreover, in panels (k) and (l) the states of high transmission are found where the sign of ε is opposed to the sign of ε_0 , which is where one usually would expect the hole states to be. In summary, we

conclude that in the p -wave junction electron- and hole-like ABS have switched places and we call these inverted ABS.

The band inversion can also be found analytically. For this purpose, we consider the self-energies from Eq. (8) in the low-energy limit $\varepsilon/\Delta \ll 1$:

$$\Sigma_S^s \approx \begin{pmatrix} 0 & \tilde{\Gamma}(e^{i\phi} + 1) \\ \tilde{\Gamma}(e^{-i\phi} + 1) & 0 \end{pmatrix}, \quad (18a)$$

$$\Sigma_S^p \approx -\frac{\Delta}{\varepsilon} \begin{pmatrix} -2\tilde{\Gamma} & \tilde{\Gamma}(e^{i\phi} - 1) \\ \tilde{\Gamma}(e^{-i\phi} - 1) & -2\tilde{\Gamma} \end{pmatrix}, \quad (18b)$$

where we used gauge freedom to set $\varphi_1 = \phi$ and $\varphi_2 = 0$. With that we find for the low-energy expressions for the EC transmission functions to be (see Appendix C)

$$T_{\text{EC}}^s(\varepsilon) \approx \frac{(\varepsilon + \varepsilon_0)^2 + 4\Gamma^2}{\mathcal{D}^s(\varepsilon^2, \varepsilon_0^2, \phi)}, \quad (19a)$$

$$T_{\text{EC}}^p(\varepsilon) \approx \frac{(\varepsilon^2 + \varepsilon\varepsilon_0 - 2\tilde{\Gamma}\Delta)^2 + 4\varepsilon^2\Gamma^2}{\mathcal{D}^p(\varepsilon^2, \varepsilon_0^2, \phi)}, \quad (19b)$$

where we set $\Gamma_L = \Gamma_R \equiv \Gamma$ and $\Gamma_1 = \Gamma_2 \equiv \tilde{\Gamma}$. Since the denominators \mathcal{D}^α , which are explicitly given in Appendix C in Eq. (C5), only depend on ε^2 and ε_0^2 , it becomes clear that T_{EC}^s reaches its maximum when ε and ε_0 have the same sign. Contrary to this, T_{EC}^p takes maximal value when ε and ε_0 have opposite sign due to the $(\varepsilon^2 + \varepsilon\varepsilon_0 - 2\tilde{\Gamma}\Delta)^2 \approx (\varepsilon\varepsilon_0 - 2\tilde{\Gamma}\Delta)^2$ term (the ε^2 term is small in the low-energy limit). As seen from the analytical calculation, this differing behavior in sign originates from the Δ/ε term in the induced gap Δ_{ind}^p given in Eq. (9b), which itself comes from the presence of Majorana zero modes at the boundaries of the topological SC wire [24]. Therefore, the inversion of Andreev bands is a signature of Majorana zero modes.

IV. TRANSPORT OBSERVABLES

In this section, we turn our attention to the previously introduced transport observables, namely the electrical conductance G , the thermal conductance K , and the Seebeck coefficient S . We are looking for fingerprints of the different symmetries of the induced gaps in s - and p -wave junctions, as well as the presence of the protected Majorana mode and the band inversion in the topological junction.

A. Electrical and heat conductance

We start by analyzing the electrical conductance G , which is shown in the first row in Fig. 4 as a function of phase difference ϕ and dot level ε_0 . There are several remarkable features that allow us to distinguish between the two junctions: The s -wave conductance shows

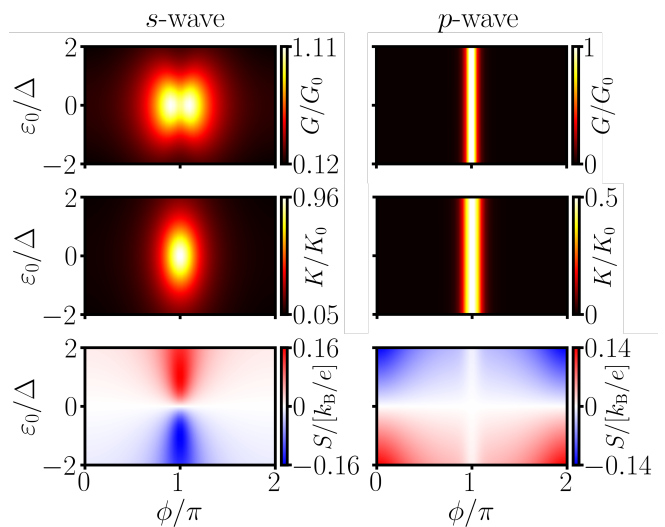


FIG. 4. Transport coefficients G , K , and S as functions of phase difference ϕ and dot level ε_0 . Parameters: $\Gamma_{1,2} = 2\Delta$, $\Gamma_{L,R} = 0.5\Delta$, $\eta = 0.001\Delta$, $k_B T = 0.01\Delta$, and $\mu = 0$.

a kidney-like structure with two peaks located at $\varepsilon_0 = 0$ and slightly away from the symmetry point $\phi = \pi$. This is due to the effects of local and crossed Andreev reflection, which both reach their maximal transmission slightly left and right from $\phi = \pi$ while completely vanishing in the center, cf. Fig. 2 (m). As discussed above, the behavior of the AR transmission is directly linked to the phase dependence of the induced gap $\Delta_{\text{ind}}^s(\phi)$, which also vanishes at $\phi = \pi$. Therefore, the kidney structure of the electrical conductance is an indicator of s -wave pairing symmetry.

In order to obtain a better insight into the functional dependencies of G^s , we can analytically compute the conductance in a low-temperature limit by applying a Sommerfeld expansion. From the result given in Appendix D in Eq. (D3a), we can read off two special cases with $\phi = 0$ and $\phi = \pi$:

$$G^s(\phi = 0)/G_0 = 4\Gamma^2 \frac{\varepsilon_0^2 + 4\Gamma^2 + 12\tilde{\Gamma}^2}{(\varepsilon_0^2 + 4\Gamma^2 + 4\tilde{\Gamma}^2)^2}, \quad (20a)$$

$$G^s(\phi = \pi)/G_0 = \frac{4\Gamma^2}{\varepsilon_0^2 + 4\Gamma^2}. \quad (20b)$$

The first observation from above equations is that for $\phi = \pi$, the conductance becomes independent of $\tilde{\Gamma}$, which is the coupling to the superconducting leads. This is due to the vanishing of the induced gap, making the SCs effectively invisible for the quantum dot. What remains is the usual conductance of a resonant tunneling model with normal-lead coupling Γ , closing the circle to our initial observations made in Fig. 1 (c) and the discussion thereof. As in the resonant tunneling model, the conductance reaches unity at $\varepsilon_0 = 0$, indicating perfect transmission. In contrast, for $\phi = 0$ the conductance depends on the couplings $\tilde{\Gamma}$, leading to a significantly suppressed

electrical transport. The analytical results are shown in the cyan dashed curves in Fig. 5. Comparison with the numerical results (blue solid curves) proves that the low-energy limit yields reliable values for the conductance. The only exception is found around $\phi = \pi$ and $\varepsilon_0 = 0$, where the numerical values are slightly below unity due to the finite temperature of $k_B T = 0.01\Delta$.

Also for the p -wave case analytical results can be found by using Eq. (D4a) in Appendix D:

$$G^p(\phi = 0)/G_0 = 0, \quad (21a)$$

$$G^p(\phi = \pi)/G_0 = 1. \quad (21b)$$

The quantized value of the conductance for $\phi = \pi$ is a result of the protected zero-energy mode and has been discussed extensively in the literature [2, 3, 24]. However, also the perfectly vanishing conductance at $\phi = 0$ is an indicator of Majorana modes: First of all, the induced gap Δ_{ind}^p vanishes at this point, prohibiting AR and CAR processes. Moreover, as one can see in the self-energy in Eq. (8b), the system then behaves like a resonant tunneling model with self-energy

$$\Sigma^p(\phi = 0) = -2 \left(\tilde{\Gamma} \sqrt{\Delta^2 - \varepsilon^2/\varepsilon + i\Gamma} \right) \tau_0. \quad (22)$$

The $1/\varepsilon$ -term stems from the presence of Majorana modes at the boundaries of the topological superconductors and appears eventually in the denominator \mathcal{D}^p given in Eq. (C5b), making the denominator diverge and the conductance vanish. In summary, while the quantized conductance at $\phi = \pi$ is a footprint of the Majorana bound state in the topological Josephson junction, the vanishing conductance at $\phi = 0$ indicates the presence of Majorana modes at the superconductors forming said junction. Lastly, comparing the orange dashed curve with the red solid curve in Fig. 5 shows a perfect match between analytical and numerical results in the p -wave conductance.

Since at low temperatures, both the electrical and heat conductance are proportional to the transmission, the heat transport yields a very similar picture as the electrical transport. However, since the transmission functions for the two processes differ (there is no contribution from local Andreev reflection to heat transport, see Eq. (14)), there are a few differences. First of all, as we can observe in Fig. 4, the heat conductance in the s -wave case shows no longer the kidney structure that we have seen in the electrical transport, due to the missing Andreev contribution. Since the electrical conductance is determined by $G/G_0 \approx T_{\text{EC}} + T_{\text{CAR}} + 2T_{\text{AR}}$ while the heat conductance is given by $K/K_0 \approx T_{\text{EC}} + T_{\text{CAR}}$ [cf. Eq. (14)], the comparison between G and K allows to filter out the Andreev reflection from the transport. Since in our case $T_{\text{CAR}} = T_{\text{AR}}$, this also makes it possible to extract the pure EC contribution to the electrical and heat transport. This we will use below when we consider the differential conductance.

The missing AR contribution is also clearly visible in the p -wave case: Although the overall structure of K^p

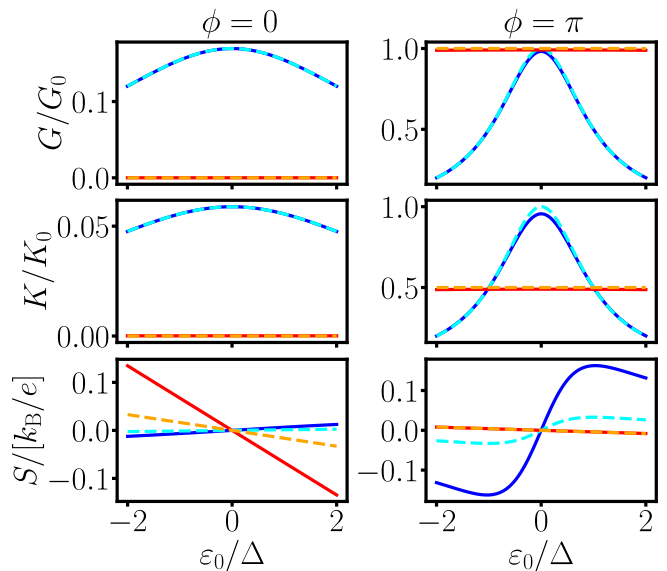


FIG. 5. Transport coefficients G , K , and S for fixed phases ϕ as functions of ε_0 . The blue and red solid curves are the numerical results for s - and p -wave, respectively, while the cyan and orange dashed curves are computed analytically. Parameters: $\Gamma_{1,2} = 2\Delta$, $\Gamma_{L,R} = 0.5\Delta$, $\eta = 0.001\Delta$, $k_B T = 0.01\Delta$, and $\mu = 0$.

is similar to the electrical conductance, the heat conductance at $\phi = \pi$ is quantized to a value of $K_0/2$ rather than the full heat conductance quantum. This is in agreement with the results presented in Ref. [21], where also a half-quantized heat conductance in a transverse topological Josephson junction has been predicted. With our analysis we have shown that the half-quantized value consists of equal parts of EC and CAR contributions.

B. Seebeck coefficient

While electrical and heat conductance are both determined by the transmission at the chemical potential and, as we have seen, give mostly the same information, the Seebeck coefficient can provide new insights. Since the Onsager coefficient L_{12} is determined by the derivative of the transmission function (cf. Appendix D), the thermopower contains information about particle-hole asymmetries in the system. Therefore, we can expect to see fingerprints of the band inversion in the thermoelectric transport.

The last row of Fig. 4 shows the Seebeck coefficient for s - and p -wave junctions. Even though the two pictures look fairly different on first glance, they are actually quite similar except for two major elements: In comparison to the s -wave case, the p -wave result appears (a) to be phase shifted by a factor of π and (b) to have the opposite sign. In short we can observe that $S^p(\phi) \approx -S^s(\phi + \pi)$.

This phase shift we have already observed in the conductances and can again be traced back to the phase

shift in the induced gap, which itself is a consequence of the different pairing symmetries in s - and p -wave superconductors. The sign change however is a new observation: Normally, like in the resonant tunneling model, for a positive dot level we would expect the thermoelectric current to be dominated by electrons as they are energetically closer to the energy of the scatterer. In that case, the Seebeck coefficient would be positive. Similarly, if $\varepsilon_0 < 0$, the current would be mainly carried by holes and, therefore, the thermopower would be negative. This is exactly the picture that we can see in the s -wave junction: $\text{sgn}(S^s(\varepsilon_0)) = \text{sgn}(\varepsilon_0)$.

In the p -wave junction we observe the opposite behavior, i.e., $\text{sgn}(S^p(\varepsilon_0)) = -\text{sgn}(\varepsilon_0)$. This indicates that at positive dot levels the states are more hole-like, while the electron-like states are found at negative energies, proving that the Andreev bands are indeed inverted. In order to get some analytical insight, we can use that at low temperatures we have $S \sim L_{12} \sim \frac{\partial T_{12}}{\partial \varepsilon}$, giving us (cf. Appendix D)

$$S^s/[k_B/e] = \frac{\pi^2}{3} k_B T \frac{2\varepsilon_0}{\varepsilon_0^2 + 4\Gamma^2 + 12\tilde{\Gamma}^2 \cos^2(\phi/2)}, \quad (23a)$$

$$S^p/[k_B/e] = \frac{\pi^2}{3} k_B T \frac{-\varepsilon_0}{\tilde{\Gamma}\Delta(1 + 3\sin^2(\phi/2))}, \quad (23b)$$

with $\mu = 0$ and therefore we have $S^s \propto \varepsilon_0$ and $S^p \propto -\varepsilon_0$.

In the last row of Fig. 5 we compare the analytical and numerical results for S^α at two different phases. At $\phi = 0$, the values for $\alpha = s$ (blue solid and cyan dashed curves) match quite well and show the expected linear behavior $\propto \varepsilon_0$. In contrast, the analytical and numerical values for S^p (red solid and orange dashed curves) do not match, although showing the same qualitative behavior. The opposite pattern can be observed at $\phi = \pi$: Here, the p -wave values match very well, while the s -wave curves strongly deviate from each other.

In order to obtain the analytical results for the Seebeck coefficient, we applied two approximations: The low-energy approximation leading to the simplified self-energies in Eq. (18) and the Sommerfeld expansion, which can be used at sufficiently low temperatures. It is easy to check that lowering the temperature does not lead to a better match between analytical and numerical results, which is why the origin of this mismatch has to lie in the low-energy approximation. What the low-energy approximation effectively does is to ignore the presence of the quasiparticle continuum above the superconducting gap. Since the Seebeck coefficient is mainly determined by the derivative of the transmission function, it also takes energies into account which deviate from 0. Therefore, unlike the conductances, which only depend on the transmission at zero energy and, therefore, are not influenced by the presence or absence of above-gap quasiparticles, the thermopower can strongly change if the quasiparticles are removed. However, as Fig. 5 shows, the analytical results still give the correct qualitative behavior.

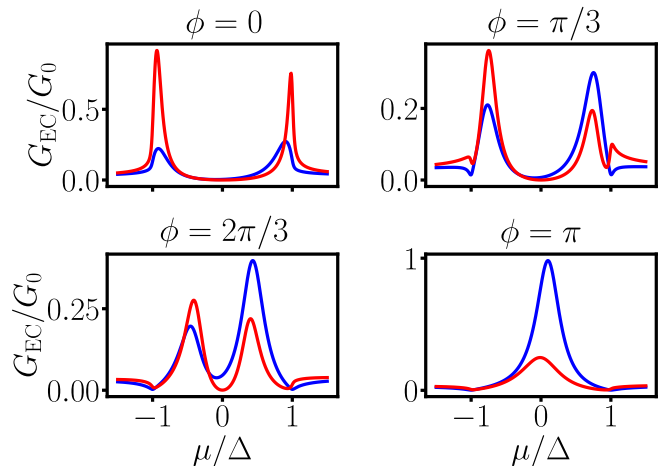


FIG. 6. Differential conductance G_{EC}^α for different values of ϕ and $\varepsilon_0 = \Delta/2$. The blue (red) curves correspond to $\alpha = s$ ($\alpha = p$). Other parameters: $\Gamma_{1,2} = 2\Delta$, $\Gamma_{L,R} = 0.5\Delta$, $\eta = 0.001\Delta$, and $k_B T = 0.01\Delta$.

C. Differential conductance

A second method to detect the band inversion is to measure the differential conductance, i.e., the conductance as a function of the reference chemical potential μ . Since band inversion is clearly visible in the EC transmission in Fig. 3 and the conductance in turn is, at low temperatures, solely determined by the transmission evaluated at the chemical potential, the differential conductance allows us to directly measure the transmission and, therefore, should reveal the band inversion. As we have argued above, by measuring both the electrical and heat conductance we can approximately determine the contribution of AR processes, which enables the extraction of the more interesting EC conductance G_{EC}^α , i.e., the contribution to the conductance originating from EC only.

The numerical results are shown in Fig. 6. Note that since the analytical results obtained in Appendix D used a low-energy approximation, these expressions are only valid for chemical potentials close to 0. Therefore we will only discuss the numerical results here. As one can see in Fig. 6, for phases $\phi \neq 0$ the conductance always has a double peak structure with one peak higher than the other. Since a conductance peak shows us at which energies the electronic states on the quantum dot are located, in a normal resonant tunneling model one would expect a single conductance peak around the dot level ε_0 . However, due to the mixing of particles and holes due to the superconductors, there are also electron-like states at negative energies, although less pronounced. Therefore, the higher peak tells us, at what energies we find the electronic states.

In all three plots in Fig. 6 which show a double-peak structure, the higher peak for the s -wave junction is found at positive chemical potentials, while in the p -

wave case we find them at negative energies. This proves again that in the topological junction the electronic states and the holes have switched their energetic positions and, therefore, the Andreev bands are inverted. Another observation that one can make is that the peaks move towards each other when tuning the phase away from 0 until eventually merging at $\phi = \pi$. This is due to the fact that the Andreev bound states also approach (cross) each other in the s -wave (p -wave) junction, cf. Fig. 2. At $\phi = \pi$ the conductance peak for the p -wave case is located at zero energy (where we expect the Majorana bound state to be), while the s -wave peak is moved slightly away from $\mu = 0$, showing that the zero-energy state in the topological junction is protected while the gap is opened in the s -wave junction.

V. CONCLUSIONS

We have studied the transport signatures in a four-terminal junction consisting of two normal metal leads and two superconductors coupled to a central quantum dot. We were interested in the transverse thermoelectric transport between the normal leads, i.e., transverse to the formed Josephson junction, enabling us to look into the Andreev bound states forming on the dot. We have chosen the SC leads to have either s -wave or p -wave pairing in order to compare topological JJs with conventional ones. We have shown how the physics of the ABS can be fully understood from the induced pairing $\Delta_{\text{ind}}^\alpha$, which, depending on the pairing symmetry of the superconductors, depends differently on the phase bias. Evidence of different phase dependencies of the induced gap can be found in the electrical conductance, cf. Fig. 4. This yields a possibility to classify the junction.

We studied the local density of states and observed the well-known protected crossing of the ABS in the p -wave junction. By looking at the transmission functions corresponding to transverse cotunneling and Andreev reflection processes, we made two things visible: The Andreev transmission mirrors well the dependencies of the induced gap function, especially the points where the induced gap vanishes, leading to a vanishing transmission. On the other hand, the EC transmission showed that the electron and hole states in the topological junction are interchanged, while the Andreev bands in the s -wave case behave quite naturally, cf. Fig. 3. In analogy to the band inversion in topological materials (see, e.g., Refs. [31, 32]) we called this phenomenon inverted Andreev bands.

We have found evidence of the band inversion in two observables: the Seebeck coefficient and the differential conductance. For the Seebeck coefficient we have found that, in the p -wave case, an anomalous sign change occurs as opposed to the s -wave case. This anomalous Seebeck effect has been found before in QD structures containing Majorana zero modes (see, e.g., Refs. [18–20]), but no explanation has been given so far. With the inversion of Andreev bands in topological junctions we have found

an intuitive explanation for this effect. The occurrence of the anomalous Seebeck effect in Refs. [18–20] involving Majorana zero modes also leads to the conclusion that band inversion on the quantum dot is a necessary condition for the presence of Majorana bound states.

It has been pointed out in several works that the anomalous Seebeck effect is no sufficient condition for the presence of MZMs as there are also other effects like Cooper-pair splitting [9] or correlations [33] that can lead to the observed sign change without involving Majoranas. Therefore, future works might concentrate on the precise conditions for the occurrence of the anomalous Seebeck effect and how it can be utilized (perhaps in combination with other effects) for the unambiguous detection of Majorana zero modes.

ACKNOWLEDGMENTS

We acknowledge funding by the Deutsche Forschungsgemeinschaft (DFG, German Research Foundation) through SFB1170 ToCoTronics, Project-ID 258499086, through the Würzburg-Dresden Cluster of Excellence in Complexity and Topology in Quantum Matter – ct.qmat (EXC2147, Project-ID 390858490)

Appendix A: Derivation of the transmission functions

In this appendix, we will show how to derive the exact expressions of the transmission functions given in Eq. (15). As stated in the main text, we start from the Heisenberg equation of motion to derive an expression for the electrical current:

$$I_L(t) = \frac{e}{i\hbar} \langle [H, N_L] \rangle (t) \quad (\text{A1a})$$

$$= \frac{e}{\hbar} t_L \sum_{\sigma} \left(i \langle c_{L\sigma}^\dagger c_{0\sigma} \rangle - i \langle c_{0\sigma}^\dagger c_{L\sigma} \rangle \right), \quad (\text{A1b})$$

where $N_L = \sum_{\sigma} c_{L\sigma}^\dagger c_{L\sigma}$ is the particle number operator of the left lead and H is the Hamiltonian defined in Eq. (1). All operators in the equation above are assumed to be time-dependent in the Heisenberg picture. By invoking the definition of the lesser Green's function,

$$G_{ij}^<(t, t') = i \langle \psi_j^\dagger(t') \otimes \psi_i(t) \rangle, \quad (\text{A2})$$

where $\psi_i^\dagger = (c_{i\uparrow}^\dagger, c_{i\downarrow})$ ($i \in \{L, R, 1, 2, 0\}$) are the Nambu spinors used in the main text, we can write the current in Fourier space as

$$I_L = \frac{e}{\hbar} t_L \int_{-\infty}^{\infty} d\varepsilon \text{tr} \left(G_{0L}^<(\varepsilon) - G_{L0}^<(\varepsilon) \right). \quad (\text{A3})$$

Note that we can safely Fourier transform the Green's function since we do not apply any voltage bias to the superconductors, which is why we achieve a steady current

without driving the system into a fully non-equilibrium state.

We can further rewrite the lesser Green's functions by using the Dyson equations [23]

$$G_{0L}^< = G_{00}^r V_{0L} g_{LL}^< + G_{00}^< V_{0L} g_{LL}^a, \quad (\text{A4a})$$

$$G_{L0}^< = g_{LL}^< V_{L0} G_{00}^a + g_{LL}^r V_{L0} G_{00}^<. \quad (\text{A4b})$$

This now allows us to apply the relations $G_{ii}^a - G_{ii}^r = G_{ii}^< - G_{ii}^>$ [23], which yields

$$I_L = \frac{e}{h} t_L^2 \int_{-\infty}^{\infty} d\varepsilon \text{tr} \left[\tau_3 (G_{00}^> g_{LL}^< - G_{00}^< g_{LL}^>) \right], \quad (\text{A5})$$

where τ_3 is the third Pauli matrix and the trace tr runs over the particle-hole degrees of freedom. In order to replace the dressed greater and lesser Green's functions with the easier to handle retarded and advanced Green's functions, we use the Dyson equation [23]

$$G_{00}^{\langle, \rangle} = \sum_{i=L,R,1,2,0} (1 + G^r V)_{0i} g_{ii}^{\langle, \rangle} (1 + V G^a)_{i0}. \quad (\text{A6})$$

Recalling that the Green's functions $g_{ii}^{\langle, \rangle}$ are proportional to the equilibrium local density of states in site i and since we are only interested in the subgap transport, we can neglect the terms with $i = 1, 2$. Furthermore, one can show that also the term proportional to $g_{00}^{\langle, \rangle}$ vanishes [23], which leaves us only two terms to evaluate. Using that $g_{ii}^< = 2\pi i \nu_0 \text{diag}(f_i^e, f_i^h)$ and $g_{ii}^> = -2\pi i \nu_0 (1 - \text{diag}(f_i^e, f_i^h))$ for $i = L, R$, one finds after some algebra

$$I_L = \frac{2e}{h} 4\Gamma_L \int_{-\infty}^{\infty} d\varepsilon \left[\Gamma_L |G_{00}^{\text{eh}}|^2 (f_L^e - f_L^h) \right] \quad (\text{A7a})$$

$$+ \Gamma_R |G_{00}^{\text{ee}}|^2 (f_L^e - f_R^e) \quad (\text{A7b})$$

$$+ \Gamma_R |G_{00}^{\text{eh}}|^2 (f_L^e - f_R^h)]. \quad (\text{A7c})$$

From this Landauer-type formula we can now read out the expressions for the transmission functions given in Eq. (15). Note that in this derivation we explicitly took into account the spin, leading to the prefactor of 2 in the Landauer formula, which is left out in the spinless case.

Appendix B: Derivation of the Onsager coefficients

With the Landauer formula found in Eq. (A7), we can now derive the exact expression of the Onsager coefficients given in Eq. (13). We start by noting that one can derive a similar Landauer formula as Eq. (A7) for the heat current by starting from the equation of motion

$$J_L(t) = -\frac{1}{i\hbar} \langle [H, H_L - \mu_L N_L] \rangle (t) \quad (\text{B1})$$

and following the same steps as above for the electrical current, leading to

$$J_L = \frac{1}{h} \int_{-\infty}^{\infty} d\varepsilon (\varepsilon - \mu_L) \left[T_{\text{AR}}^\alpha (f_L^e - f_L^h) \right] \quad (\text{B2a})$$

$$+ T_{\text{EC}}^\alpha (f_L^e - f_R^e) \quad (\text{B2b})$$

$$+ T_{\text{CAR}}^\alpha (f_L^e - f_R^h)]. \quad (\text{B2c})$$

The Fermi functions are given by

$$f_i^{e/h}(\varepsilon) = \left(1 + \exp\left(\frac{\varepsilon \mp \mu_i}{k_B T_i}\right) \right)^{-1}, \quad (\text{B3})$$

with $i \in \{L, R\}$. By choosing $\mu_L = \mu + \Delta\mu$ and $\mu_R = \mu$ as well as $T_L = T + \Delta T$ and $T_R = T$ in accordance with the main text, we can linearize the Landauer formulas assuming $\Delta\mu$ and ΔT to be small. This eventually leads to the linear Onsager relation in Eq. (12) with the coefficients given in Eq. (13).

Appendix C: Low-energy expressions of the transmissions

To find the low-energy limits of the transmission functions we start by noting that if $\varepsilon/\Delta \ll 1$, we have

$$\frac{\Delta}{\sqrt{\Delta^2 - \varepsilon^2}} \approx 1, \quad \tilde{\varepsilon} = \frac{\varepsilon}{\sqrt{\Delta^2 - \varepsilon^2}} \approx 0, \quad (\text{C1})$$

leading to the self-energies in Eq. (18). In the s -wave case, the Green's function is then given by (cf. Eq. (6))

$$G_0^s \approx \begin{pmatrix} \varepsilon - \varepsilon_0 + 2i\Gamma & -\tilde{\Gamma}(e^{i\phi} + 1) \\ -\tilde{\Gamma}(e^{-i\phi} + 1) & \varepsilon + \varepsilon_0 + 2i\Gamma \end{pmatrix}^{-1} \quad (\text{C2})$$

By explicitly calculating the inverse and using definition in Eq. (15), we find

$$T_{\text{EC}}^s = 4\Gamma^2 |G_0^{s,\text{ee}}|^2 = \frac{(\varepsilon + \varepsilon_0)^2 + 4\Gamma^2}{\mathcal{D}^s(\varepsilon^2, \varepsilon_0^2, \phi)}, \quad (\text{C3a})$$

$$T_{\text{AR}}^s = 4\Gamma^2 |G_0^{s,\text{eh}}|^2 = \frac{4\tilde{\Gamma}^2 \cos^2(\phi/2)}{\mathcal{D}^s(\varepsilon^2, \varepsilon_0^2, \phi)}. \quad (\text{C3b})$$

In the same way we can calculate the transmissions in the p -wave case, which are given by

$$T_{\text{EC}}^p = \frac{(\varepsilon^2 + \varepsilon\varepsilon_0 - 2\tilde{\Gamma}\Delta)^2 + 4\varepsilon^2\Gamma^2}{\mathcal{D}^p(\varepsilon^2, \varepsilon_0^2, \phi)}, \quad (\text{C4a})$$

$$T_{\text{AR}}^p = \frac{4\Delta^2\tilde{\Gamma}^2 \sin^2(\phi/2)}{\mathcal{D}^p(\varepsilon^2, \varepsilon_0^2, \phi)}, \quad (\text{C4b})$$

where the denominators are given by

$$\mathcal{D}^s(\varepsilon^2, \varepsilon_0^2, \phi) = \frac{1}{4\Gamma^2} \left((\varepsilon^2 - \varepsilon_0^2 - 4\Gamma^2 - 4\tilde{\Gamma}^2 \cos^2(\phi/2))^2 + 16\varepsilon^2\Gamma^2 \right), \quad (\text{C5a})$$

$$\mathcal{D}^p(\varepsilon^2, \varepsilon_0^2, \phi) = \frac{\varepsilon^2}{4\Gamma^2} \left((m(\varepsilon)^2 - 4\Gamma^2 - \varepsilon_0^2 - 4\Delta^2\tilde{\Gamma}^2 \sin^2(\phi/2)/\varepsilon^2)^2 + 16\Gamma^2 m(\varepsilon)^2 \right), \quad (\text{C5b})$$

with $m(\varepsilon) = \varepsilon - 2\Delta\tilde{\Gamma}/\varepsilon$.

Sommerfeld expansion, resulting in

$$L_{11} \approx \mathbf{T}_{11}(\mu), \quad (\text{D1a})$$

$$L_{12} \approx \frac{\pi^2}{3} k_B T \frac{\partial \mathbf{T}_{12}}{\partial \varepsilon}(\mu) = L_{21}, \quad (\text{D1b})$$

$$L_{22} \approx \frac{\pi^2}{3} \mathbf{T}_{22}(\mu). \quad (\text{D1c})$$

The derivative of the transmission function needed for the L_{12} coefficient is given by

Appendix D: Low-temperature expansion of the transport coefficients

$$\left. \frac{\partial \mathbf{T}_{12}^s}{\partial \varepsilon} \right|_{\varepsilon=0} = \frac{2\varepsilon_0}{\mathcal{D}^s(0)}, \quad (\text{D2a})$$

$$\left. \frac{\partial \mathbf{T}_{12}^p}{\partial \varepsilon} \right|_{\varepsilon=0} = -\frac{4\tilde{\Gamma}\Delta\varepsilon_0}{\mathcal{D}^p(0)}, \quad (\text{D2b})$$

At sufficiently low temperatures, we can approximate the Onsager coefficients given in Eq. (13) by means of a

where we used that $\mathbf{T}_{12}^\alpha = \mathbf{T}_{\text{EC}}^\alpha + \mathbf{T}_{\text{CAR}}^\alpha$.

With that, we find the analytical expressions for the transport coefficients in s -wave case to be

$$G^s/G_0 = \frac{(\mu + \varepsilon_0)^2 + 4\Gamma^2 + 12\tilde{\Gamma}^2 \cos^2(\phi/2)}{\mathcal{D}^s(\mu^2, \varepsilon_0^2, \phi)}, \quad (\text{D3a})$$

$$S^s/[k_B/e] = \frac{\pi^2}{3} k_B T \frac{2\varepsilon_0}{\varepsilon_0^2 + 4\Gamma^2 + 3 \cdot 4\tilde{\Gamma}^2 \cos^2(\phi/2)} \quad (\mu = 0), \quad (\text{D3b})$$

$$K^s/K_0 \approx \frac{(\mu + \varepsilon_0)^2 + 4\Gamma^2 + 4\tilde{\Gamma}^2 \cos^2(\phi/2)}{\mathcal{D}^s(\mu^2, \varepsilon_0^2, \phi)}, \quad (\text{D3c})$$

where for the heat conductance we used that the term L_{12}^2/L_{11} is small compared to L_{22} for sufficiently low temperatures. Note that for the Seebeck coefficient we put $\mu = 0$ for simplicity. For the p -wave case we find

$$G^p/G_0 = \frac{(\mu^2 + \mu\varepsilon_0 - 2\tilde{\Gamma}\Delta)^2 + 4\mu^2\Gamma^2 + 12\Delta^2\tilde{\Gamma}^2 \sin^2(\phi/2)}{\mathcal{D}^p(\mu^2, \varepsilon_0^2, \phi)}, \quad (\text{D4a})$$

$$S^p/[k_B/e] = -\frac{\pi^2}{3} k_B T \frac{\varepsilon_0}{\tilde{\Gamma}\Delta(1 + 3\sin^2(\phi/2))} \quad (\mu = 0), \quad (\text{D4b})$$

$$K^p/K_0 \approx \frac{(\mu^2 + \mu\varepsilon_0 - 2\tilde{\Gamma}\Delta)^2 + 4\mu^2\Gamma^2 + 4\Delta^2\tilde{\Gamma}^2 \sin^2(\phi/2)}{\mathcal{D}^p(\mu^2, \varepsilon_0^2, \phi)}. \quad (\text{D4c})$$

- [1] A. Y. Kitaev, Unpaired Majorana fermions in quantum wires, *Physics-Uspekhi* **44**, 131 (2001).
 [2] K. T. Law, P. A. Lee, and T. K. Ng, Majorana Fermion Induced Resonant Andreev Reflection, *Phys. Rev. Lett.*

- 103**, 237001 (2009).
 [3] K. Flensberg, Tunneling characteristics of a chain of Majorana bound states, *Phys. Rev. B* **82**, 180516 (2010).
 [4] J. D. Sau, S. Tewari, R. M. Lutchyn, T. D. Stanescu, and

- S. Das Sarma, Non-Abelian quantum order in spin-orbit-coupled semiconductors: Search for topological Majorana particles in solid-state systems, *Phys. Rev. B* **82**, 214509 (2010).
- [5] V. Mourik, K. Zuo, S. M. Frolov, S. R. Plissard, E. P. A. M. Bakkers, and L. P. Kouwenhoven, Signatures of Majorana Fermions in Hybrid Superconductor-Semiconductor Nanowire Devices, *Science* **336**, 1003 (2012).
- [6] C. Moore, T. D. Stanescu, and S. Tewari, Two-terminal charge tunneling: Disentangling Majorana zero modes from partially separated Andreev bound states in semiconductor-superconductor heterostructures, *Phys. Rev. B* **97**, 165302 (2018).
- [7] A. Vuik, B. Nijholt, A. R. Akhmerov, and M. Wimmer, Reproducing topological properties with quasi-Majorana states, *SciPost Phys.* **7**, 061 (2019).
- [8] P. Yu, J. Chen, M. Gomanko, G. Badawy, E. P. A. M. Bakkers, K. Zuo, V. Mourik, and S. M. Frolov, Non-Majorana states yield nearly quantized conductance in proximatized nanowires, *Nature Physics* **17**, 482 (2021).
- [9] R. L. Klees, D. Gresta, J. Sturm, L. W. Molenkamp, and E. M. Hankiewicz, Majorana-mediated thermoelectric transport in multiterminal junctions, *Phys. Rev. B* **110**, 064517 (2024).
- [10] L. Fu and C. L. Kane, Superconducting Proximity Effect and Majorana Fermions at the Surface of a Topological Insulator, *Phys. Rev. Lett.* **100**, 096407 (2008).
- [11] G. Tkachov and E. M. Hankiewicz, Helical andreev bound states and superconducting klein tunneling in topological insulator josephson junctions, *Phys. Rev. B* **88**, 075401 (2013).
- [12] Y. Peng, F. Pientka, E. Berg, Y. Oreg, and F. von Oppen, Signatures of topological Josephson junctions, *Phys. Rev. B* **94**, 085409 (2016).
- [13] R. S. Deacon, J. Wiedenmann, E. Bocquillon, F. Domínguez, T. M. Klapwijk, P. Leubner, C. Brüne, E. M. Hankiewicz, S. Tarucha, K. Ishibashi, H. Buhmann, and L. W. Molenkamp, Josephson Radiation from Gapless Andreev Bound States in HgTe-Based Topological Junctions, *Phys. Rev. X* **7**, 021011 (2017).
- [14] A. Zazunov, S. Plugge, and R. Egger, Fermi-Liquid Approach for Superconducting Kondo Problems, *Phys. Rev. Lett.* **121**, 207701 (2018).
- [15] C.-K. Chiu and S. Das Sarma, Fractional Josephson effect with and without Majorana zero modes, *Phys. Rev. B* **99**, 035312 (2019).
- [16] B. Sothmann and E. M. Hankiewicz, Fingerprint of topological Andreev bound states in phase-dependent heat transport, *Phys. Rev. B* **94**, 081407 (2016).
- [17] B. Scharf, A. Braggio, E. Strambini, F. Giazotto, and E. M. Hankiewicz, Topological Josephson heat engine, *Communications Physics* **3**, 198 (2020).
- [18] R. López, M. Lee, L. m. c. Serra, and J. S. Lim, Thermoelectrical detection of Majorana states, *Phys. Rev. B* **89**, 205418 (2014).
- [19] S. Valentini, R. Fazio, V. Giovannetti, and F. Taddei, Thermopower of three-terminal topological superconducting systems, *Phys. Rev. B* **91**, 045430 (2015).
- [20] I. Grosu and I. Tifrea, Thermoelectric transport properties of single quantum dot systems in the presence of Majorana states, *Physica E: Low-dimensional Systems and Nanostructures* **145**, 115503 (2023).
- [21] A. G. Bauer, B. Scharf, L. W. Molenkamp, E. M. Hankiewicz, and B. Sothmann, Quantized phase-coherent heat transport of counterpropagating Majorana modes, *Phys. Rev. B* **104**, L201410 (2021).
- [22] A. Martín-Rodero and A. L. Yeyati, Josephson and Andreev transport through quantum dots, *Advances in Physics* **60**, 899 (2011).
- [23] J. C. Cuevas and E. Scheer, *Molecular Electronics - An Introduction to Theory and Experiment* (World Scientific, 2017).
- [24] A. Zazunov, R. Egger, and A. Levy Yeyati, Low-energy theory of transport in Majorana wire junctions, *Phys. Rev. B* **94**, 014502 (2016).
- [25] R. C. Dynes, V. Narayanamurti, and J. P. Garno, Direct Measurement of Quasiparticle-Lifetime Broadening in a Strong-Coupled Superconductor, *Phys. Rev. Lett.* **41**, 1509 (1978).
- [26] J. C. Cuevas, A. Martín-Rodero, and A. L. Yeyati, Hamiltonian approach to the transport properties of superconducting quantum point contacts, *Phys. Rev. B* **54**, 7366 (1996).
- [27] G. Benenti, G. Casati, K. Saito, and R. S. Whitney, Fundamental aspects of steady-state conversion of heat to work at the nanoscale, *Physics Reports* **694**, 1 (2017).
- [28] D. S. Fisher and P. A. Lee, Relation between conductivity and transmission matrix, *Phys. Rev. B* **23**, 6851 (1981).
- [29] Z. Cao, T.-F. Fang, L. Li, and H.-G. Luo, Thermoelectric-induced unitary cooper pair splitting efficiency, *Appl. Phys. Lett.* **107**, 212601 (2015).
- [30] G. E. Blonder, M. Tinkham, and T. M. Klapwijk, Transition from metallic to tunneling regimes in superconducting microconstrictions: Excess current, charge imbalance, and supercurrent conversion, *Phys. Rev. B* **25**, 4515 (1982).
- [31] L. Fu and C. L. Kane, Topological insulators with inversion symmetry, *Phys. Rev. B* **76**, 045302 (2007).
- [32] Z. Zhu, Y. Cheng, and U. Schwingenschlögl, Band inversion mechanism in topological insulators: A guideline for materials design, *Phys. Rev. B* **85**, 235401 (2012).
- [33] F. Chi, Z.-G. Fu, J. Liu, K.-M. Li, Z. Wang, and Z. Ping, Thermoelectric effect in a correlated quantum dot side-coupled to majorana bound states, *Nanoscale Res Lett* **15**, 79 (2020).